Chem. Mater. **2005,** *17,* 315−321

Cerium L_{III}-Edge XAS Investigation of the Structure of Crystalline and Amorphous Cerium Oxides

Ahmed M. Shahin,[†] Fernande Grandjean,[†,‡] Gary J. Long,[†] and Thomas P. Schuman*,[†]

Department of Chemistry and Graduate Center for Materials Research, University of Missouri—Rolla,
Rolla, Missouri 65409-0010 and Department of Physics, B5, University of Liège,
B-4000 Sart-Tilman, Belgium

Received May 13, 2004. Revised Manuscript Received October 7, 2004

Cerium oxide solid samples were prepared via precipitation from aqueous solution of hydrous cerium(III) nitrate in the presence of different percentages of hydrogen peroxide (H_2O_2) as model corrosion inhibiting coatings materials for aluminum alloys. X-ray absorption spectroscopy at the Ce L_{III}-edge was applied for the characterization of crystalline anhydrous CeO_2, nanocrystalline hydrous CeO_2, nanocrystalline CeO_2 sample **I** precipitated in the presence of H_2O_2, and an amorphous CeO_2 sample **II** precipitated at a higher H_2O_2 concentration. An analysis by X-ray absorption near-edge structure (XANES) for cerium oxides did not indicate a broad variation in cerium valence state in the precipitated samples as compared to anhydrous CeO_2. Furthermore, XANES analysis revealed a decrease in the intensity of the white line peaks for the precipitated samples relative to those in anhydrous CeO_2. The EXAFS spectra of the oxides showed that H_2O_2 reduced the precipitate's particle diameter and bulk crystallinity. Growth in the coordination number of the first, Ce−O, shell was observed with an increased bond distance R_{Ce-O} in hydrous and precipitated CeO_2 samples. However, the coordination numbers of the second, Ce−Ce, and third, Ce−O, shells were reduced in comparison with anhydrous CeO_2. Increasing concentration of H_2O_2 during alkaline precipitation of cerium oxides caused increased hydration, corresponding to a reduced outer-shell coordination number and reduced bulk crystallinity but no corresponding change in the cerium valence state.

Introduction

As a consequence of changing properties, e.g., mechanical, magnetic, or electrical, the nanocrystalline phase of rare earth metal oxides has become of immense interest.[1−4] Of these, cerium oxides have attracted considerable research interest due to a diversity of applications. For instance, the basicity function of cerium oxide when combined with the hydrogenation property of a metal such as Pt or Pd denotes cerium oxide as a promising conversion catalyst. Thus, cerium oxide can lead to selective hydrogenation catalysis of unsaturated compounds.[5,6] Of modern interest is the ability of the cerium oxide to store and transport oxygen. The phenomenon is associated with a fast valence change in the solid, i.e., $Ce^{IV} \leftrightarrow Ce^{III}$, and also with anionic vacancies, $CeO_2 \rightarrow CeO_{2-x} + (x/2)O_2$.[7,8]

Hinton and co-workers[9] examined the inhibition of corrosion of high tensile strength aluminum alloys by rare earth metal salts. Immersion of aluminum alloy in $CeCl_3$ aqueous solution for several days formed a cerium-rich film and provided significant corrosion inhibition upon exposure to a corrosive NaCl solution.[10−13] Surface analysis revealed incorporation of cerium into compact protective surface films. Adding several weight percent of hydrogen peroxide to a $CeCl_3$ solution resulted in improved corrosion-resistant films.[14] Corrosion protection is attributed to the formation of cerium oxide or hydroxide films containing Ce^{III} and Ce^{IV}.[15,16] Cerium(IV) oxides detected in the coating were believed to arise from oxidation of Ce^{III} in oxygenated

---

* To whom correspondence should be addressed. E-mail: tschuman@umr.edu.
[†] University of Missouri-Rolla.
[‡] University of Liège.

(1) Winterer, M.; Nitsche, R.; Hahn, H. *J. Phys. IV Fr.* **1997**, *7*, C2−1211.
(2) Nitsche, R.; Winterer, M.; Groft, M.; Hahn, H. *Nucl. Instrum. Methodol. B* **1995**, *97*, 127.
(3) Luca, V.; Djajanti, S.; Howe, R. F. *J. Phys. Chem. B* **1998**, *102*, 10650.
(4) Chen, L. X.; Rajh, R.; Wang, Z.; Thurnauer, M. C. *J. Phys. Chem. B* **1997**, *101*, 10688.
(5) Fierro, J. L. G.; Soria, J.; Sanz, J.; Rojo, M. J. *J. Solid State Chem.* **1987**, *66*, 154.
(6) Sim, K. S.; Hilaire, L.; Le Normand, F.; Touroude, R.; Paul-Boncour, V.; Percheron-Guegan, A. *J. Chem. Soc., Faraday Trans.* **1991**, *87*, 1453.
(7) Bunluesin, T.; Gorte, R. J.; Graham, G. W. *Appl Catal. B* **1997**, *14*, 984.
(8) Sun, Y.; Sermon, P. A. *J. Mater. Chem.* **1996**, *6*, 1025.
(9) Hinton, B. R. W.; Arnott, D. R.; Ryan, N. E. *Met. Forum* **1984**, *7*, 211.
(10) Groshart, E. A. Designing for Finishing, Part II—Conversion Coating. *Met. Finish.* **1984**, *82* (6), 69−70.
(11) Seon, *J. Less-Common Met.* **1989**, *148*, 73−78.
(12) Schuman, T. P. Protective Coatings for Aluminum Alloys. In *Handbook of Environmental Degradation of Materials*; Kutz, M., Ed.; William Andrew: New York, in press.
(13) Schuman, T. P.; Shahin, A.; Stoffer, J. O. *Proceedings of the International Waterborne, High Solids, and Powder Coating Symposium* **2002**, *29*, 371−382.
(14) Wilson, L.; Hinton, B. R. W. A Method of Forming a Corrosion Resistant Coating. Patent WO 88/06639.
(15) Hayes, S. A.; Yu, P.; O'Keefe, T. J.; O'Keefe, M. J.; Stoffer, J. O. *J. Electrochem. Soc.* **2002**, *148*, C253−C256.
(16) Hughes, A. E.; Taylor, R. J.; Hinton, B. R. W.; Wilson, L. *Surf. Interface Anal.* **1995**, *23*, 540−550.

10.1021/cm0492437 CCC: $30.25

alkaline solutions.[17] Use of cerium oxides as corrosion inhibitors in the deposited films has made it essential to understand their electronic and structural properties.

High-energy spectroscopic techniques, such as X-ray absorption, have been devoted to the investigation of different cerium oxides or hydroxides aiming at characterizing or identifying the predominant species.[18,19] The electronic configuration of the cerium center in its oxides has been a subject of heightened research.[20−23] Mixing of the 4f states of the cerium with the 2p states of oxygen provides a satisfactory explanation of the electronic configuration of cerium in its oxides.[22] The local atomic structure of non-stoichiometric CeO_{2-x} has also been subjected to several investigations.[24−26]

In this study, we report the synthesis of cerium oxide using precipitation conditions similar to those used in the preparation of cerium oxide films on aluminum. We also investigated the valence state of cerium ions and covalence with oxide ligands by varying the reaction conditions. Cerium is known to exhibit mixed-valence-like behavior and shows characteristic X-ray absorption near-edge structure (XANES) corresponding to the bonding between cerium and oxide ligands.[20−23] The cerium electronic configuration in the synthesized oxides was probed using XANES. Local structural features around cerium in precipitated cerium oxides were also investigated using extended X-ray absorption fine structure (EXAFS) and compared with two different commercial standards, i.e., anhydrous cerium oxide and hydrous cerium oxide.

Experimental Section

Materials. ACS-reagent or HPLC-grade solvents and chemicals were used throughout. Certified hydrogen peroxide 30% and ammonium hydroxide were obtained from Fisher Scientific. Cerium nitrate hexahydrate, $Ce(NO_3)_3{\cdot}6H_2O$, 99.5%, anhydrous cerium oxide 99%, and hydrous cerium oxide were obtained from Alfa Aesar.

Sample Preparation. A dilute aqueous ammonia solution (0.01 M) was added dropwise to a mixture of 0.05 mol of an aqueous solution of cerium nitrate hexahydrate, $Ce(NO_3)_3{\cdot}6H_2O$, and hydrogen peroxide, H_2O_2. Because oxidation by H_2O_2 is slow in acidic media, a few drops (10−20) of aqueous ammonia were added to accelerate the oxidation of Ce^{III} to Ce^{IV} and subsequent precipitation. Cerium oxide was precipitated at two different H_2O_2 concentrations. The molar ratios of cerium to H_2O_2 were 1:0.8 and 1:1.2.[27] The strongly oxidizing nature of H_2O_2 is attributed to its decomposition forming H_2O and O_2 in the presence of cerium. Addition of H_2O_2 to an aqueous solution of cerium nitrate increased the acidity of the solution to a pH of 2 as a result of the dissociation of H_2O_2 into H^+ and HO_2^-.[28]

Upon mixing, the solution turned similarly orange in color at either low or high H_2O_2 concentrations. The solutions were stirred in air at 295 K for 24 h. The solid precipitates were filtered, washed with deionized water, and then dried in a vacuum oven at 295 K. Upon exposure to the atmosphere, the color of the precipitate developed at low H_2O_2 concentration (**I**) faded from orange to greenish yellow. However, the orange color of the precipitate developed at high H_2O_2 concentration (**II**) was persistent. The precipitated samples under study were exposed to air at room temperature for 2 weeks before further study. All samples in our study were sized by grinding in a ball jar containing cylindrical 0.6 cm ZrO_2 media and classified through a 3.7×10^{-5} m mesh (#400) stainless steel screen.

X-ray Absorption Spectroscopy. *X-ray Absorption Measurements.* X-ray absorption measurements were carried out at the unfocused 4−3 beamline of the Stanford Synchrotron Radiation Laboratory (SSRL). The measurements were carried out in both transmission and fluorescence modes at room temperature. Ion chambers filled with a mixture of nitrogen and helium were installed in front of and behind the sample, which simultaneously detected the incident and transmission X-ray intensities. A Lytle detector was used to concurrently detect sample fluorescence. Higher harmonic X-ray intensities were minimized by detuning the Si(220) double-crystal X-ray monochromator.

Spectra were recorded in the range 5.5−6.2 keV, which covers the L_{III}-edge absorption of cerium. Spectra were scanned with a 10 eV step width between 5.500 and 5.710 keV, while the 5.710−6.2 keV region increment was chosen to be equidistant in k-space, with a 0.03 $Å^{-1}$ step width. The threshold was chosen as the inflection point of the most intense transition at 5.723 keV. Up to seven scans were averaged to improve the signal-to-noise ratio of the measurements.

XANES Data Analysis. A linear background was removed from the preedge and postedge regions of each spectrum, and the edge height was normalized to unity with the postedge values asymptotically approaching zero. Two different approaches were used to determine the transition energy and the width of each electronic excited state: in terms of (i) many-body configuration theory for a core transition to localized electronic states and (ii) one-electron band structure of the crystal for a core transition to delocalized electronic states.[21]

EXAFS Data Analysis. EXAFS data analysis was based on standard least-squares fitting techniques using the WINXAS program package.[29] The region to 700 eV above the Ce L_{III}-edge was investigated. The absorption curves were transformed to k-space using the formula $k = (2m(E - E_0)/\hbar^2)^{1/2}$. The ionization energy, E_0, the origin for calculation of the $\chi(k)$-function, was fixed at the maximum of the most intense absorption feature, the white line of the individual spectrum. Prior to analysis, the k^3-weighted EXAFS spectra were Fourier transformed over a k-space range of 2.5−11 $Å^{-1}$ using the symmetric square window, “Hanning sills.”

To extract the neighboring atomic distance, R, the mean square radial displacements or the Debye−Waller factors, σ^2, and the coordination numbers, N, from the EXAFS spectrum, two fitting models were employed. In the first model, the backscattering amplitude and phase-shift functions for single-scattering paths were calculated using FEFF 8.20.[30] In the second model, the backscattering amplitude, A_s (π, k) (see eq 1), and phase shift, φ_s, were

---

(17) Seah, M. P. *Surf. Interface Anal.* **1989**, *14*, 488.
(18) Sham, T. K. *J. Chem. Phys.* **1983**, *79*, 1116.
(19) Sham, T. K. *Phys. Rev. B* **1989**, *40*, 6045.
(20) Kaindl, G.; Schmiester, G.; Sampathkumaran, E. V. *Phys. Rev. B* **1988**, *38*, 10174.
(21) Soldatov, A. V.; Ivanchenko, T. S.; Della Longa, S.; Kotani, A.; Iwamoto, Y.; Bianconi, A. *Phys. Rev. B* **1994**, *50*, 5074.
(22) Hu, Z.; Bertram, S.; Kaindl, G. *Phys. Rev. B* **1994**, *49*, 39.
(23) Dexpert, H.; Karnatak, R. C.; Esteva, J. M.; Connerade, J. P.; Gasgnier, M.; Caro, P. E.; Albert, L. *Phys. Rev. B* **1987**, *36*, 1750.
(24) Tuller, H. L.; Nowick, A. S. *J. Electrochem. Soc., Solid State Sci. Technol.* **1975**, *122*, 255.
(25) Bevan, D. J. M.; Kordis, J. *J. Inorg. Nucl. Chem.* **1964**, *26*, 1509.
(26) Brauer, G.; Gingerich, K. A.; Holtzchmidt, U. *J. Inorg. Nucl. Chem.* **1960**, *16*, 77.
(27) Personal communication with Paul Yu and Scott Hayes.
(28) Cotton, F. A.; Wilkinson, G. *Basic Inorganic Chemistry;* Wiley: New York, 1976; p 375.
(29) Ressler, T. *J. Phys. IV Fr.* **1997**, *7*, C2−269.

Table 1. Parameters Extracted from the First Least-Squares Fitting Model of the EXAFS Spectra[a]

	Ce−O1 (first shell)			Ce−Ce (second shell)			Ce−O2 (third shell)		
sample	R (Å)	N_1	σ^2 (10^{-3} Å^2)	R (Å)	N_2	σ^2 (10^{-3} Å^2)	R (Å)	N_3	σ^2 (10^{-3} Å^2)
crystallographic data	2.343	8		3.826	12		4.487	24	
anhydrous CeO_2	2.341(1)	8(1)	3.20(4)	3.836(3)	12(2.1)	1.50(2)	4.479(1)	24(0.6)	2.40(1)
hydrous CeO_2	2.360(2)	9.5(1.4)	6.40(6)	3.847(4)	7.4(1.5)	3.30(8)	4.210(6)	18.3(1.4)	3.20(4)
I	2.367(3)	10(1.6)	9.60(1)	4.134(1)	6.6(1.2)	4.50(1)	4.127(20)	16.4(1.7)	5.1(4)
II	2.420(1)	11.5(1.9)	10.70(1)	3.814(7)	3.2(2.2)	10.90(2)			

[a] In this fitting model the backscattering amplitude, A_s (π, k), and phase-shift functions for single-scattering paths by N_j backscatterers in the *jth* shell were calculated using FEFF 8.20.[30]

Table 2. Parameters Extracted from the Second Least-Squares Fitting Model of the EXAFS Spectra[a]

	Ce−O1 (first shell)			Ce−Ce (second shell)			Ce−O2 (third shell)		
sample	R (Å)	N_1	σ^2 (10^{-3} Å^2)	R (Å)	N_2	σ^2 (10^{-3} Å^2)	R (Å)	N_3	σ^2 (10^{-3} Å^2)
anhydrous CeO_2	2.343[b]	8[b]	3.20(4)	3.836[b]	12[b]	1.50(2)	4.487[b]	24[b]	2.40(1)
hydrous CeO_2	2.360(2)	9.5(1)	6.45(5)	3.847(3)	7.4(1.1)	3.30(6)	4.210(5)	18.0(1.6)	3.20(5)
I	2.364(3)	10(1.5)	9.43(2)	4.122(2)	6.6(1.6)	4.20(1)	4.127(17)	16.1(1)	4.80(6)
II	2.420(1)	11.5(1.3)	10.22(6)	3.814(4)	3.6(1)	9.60(2)			

[a] In the second fitting model the backscattering amplitude, A_s (π, k) (see eq 1), and phase shift, φ_s, were extracted from the Ce L_{III}-edge reference spectrum of anhydrous CeO_2 and then used to model the EXAFS of the samples hydrous CeO_2, **I**, and **II**. [b] Fixed parameters.

extracted from the Ce L_{III}-edge reference spectrum of anhydrous CeO_2 and then substituted for those of the unknown samples.[31] All fitting operations were performed in *R*-space over the individual radial distance ranges given in Tables 1 and 2.

$$A_s(\pi,k) = S_0^{\,2}F_j(\pi,k)\exp(-2k^2\sigma_s^{\,2})\exp(-2R_s/\lambda_s) \qquad (1)$$

Equation 2 gives the EXAFS formula[32] used to fit the experimental spectra

$$\chi_j(k) = \frac{N_j S_0^{\,2}(k)}{kR_j^{\,2}}F_j(\pi,k)\exp(-2k^2\Delta\sigma_j^{\,2})\exp(-2R_j/\lambda_j(k))\sin(2kR_j + \phi_j(k)) \qquad (2)$$

where R_j is the distance between the cerium atom and N_j backscatterers in the *j*th shell, $F_j(\pi, k)$ is the effective amplitude function for each scattering path, λ_j is the mean free path of the photoelectron, φ_j is the phase shift, and $\Delta\sigma_j^2 = \sigma_{uj}^2 - \sigma_{sj}^2$ is the Debye−Waller factor where subscripts u and s stand for the unknown and the reference sample, respectively.[31] The amplitude reduction factor, S_0^2, was fixed at 0.82 to obtain the crystallographic coordination number and the bond lengths of the shells in the anhydrous CeO_2 fluorite structure.[33]

Discussion

XANES Spectral Results. The XANES spectra for anhydrous CeO_2, hydrous CeO_2, **I**, and **II** are depicted in Figure 1. The presence of mixed valence cerium at the Ce L_{III}-edge makes the X-ray absorption complex. XANES spectra of all the samples under study revealed that each major band exhibited a double white line characteristic of a mixture of the two cerium ground-state electronic configurations, $4f^0$ and $4f^1$.

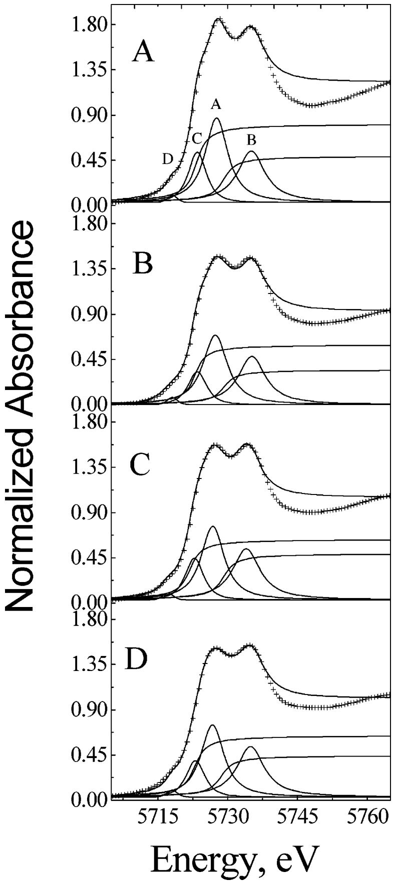

Figure 1. Ce L_{III}-edge XANES spectra with fits of (A) anhydrous CeO_2, (B) hydrous CeO_2, (C) sample **I**, and (D) sample **II**. Experimental data points are represented by (+), fitting model points by smooth curves.

Four peaks were fit in the XANES spectra, a high-energy peak A, main peak B, low-energy peak C, and preedge peak D. Peaks A and B were assigned as due to a mixture of the multielectron configurations $L4f^05d^1$ and $L4f^15d^1$, respectively, where L denotes the hole in the 2p shell and $5d^1$ refers to the excited electron in the previously unoccupied 5d state.[34]

---

(30) Ankudinov, A. L.; Bouldin, C.; Rehr, J. J.; Sims, J.; Hung, H. *Phys. Rev. B* **2002**, *65*, 104107.

(31) Wu, Z.; Benfield, R. E.; Guo, L.; Li, H.; Yang, Q.; Grandjean, D.; Li, Q.; Zhu, H. *J. Phys.: Condens. Matter* **2001**, *13*, 5269−5283.

(32) Sayers, D. E.; Bunker, B. A. X-ray Absorption: Principle. Applications and techniques of EXAFS, SEXAFS and XANES; Koningsberger, D. C., Prins, R., Eds.; Wiley: New York, 1988; Chapter 6.

(33) Lee, P. A.; Citrin, P. H.; Eisenberger, P.; Kincaid, B. M. *Rev. Mod. Phys.* **1981**, *53*, 769−806.

(34) Bianconi, A.; Marcelli, A.; Dexpert, H.; Karnatak, R.; Kotani, A.; Jo, T.; Petiau, J. *Phys. Rev. B* **1987**, *35*, 806.

Table 3. Cerium L_{III}-Edge XANES Fits of the Two Characteristic Peaks

sample	peak A position (eV)	peak A width (eV)	peak B position (eV)	peak B width (eV)	*f*-electron population	valence least-squares fitting	FEFF 8.20 calculated valence
anhydrous CeO_2	5735.1	3.5	5727.6	2.8	0.55	3.45	3.48
hydrous CeO_2	5735.2	3.2	5727.1	2.9	0.49	3.51	3.49
I	5734.3	3.6	5726.5	3.0	0.53	3.47	3.51
II	5734.7	3.8	5726.5	3.2	0.52	3.48	3.52

The feature D in the preedge region is a result of the dipole-forbidden $2p_{3/2} \rightarrow 4f$ transition, which is a consequence of a 5d admixture with the 4f state.[34] The Ce 5d states are split in the cubic crystal field of the oxygen, resulting in the low-energy shoulder, C.[21] Integration of peak C at ~5723 eV displayed a different area for each of the samples. On the basis of this and other[35] observations, the electronic transition that occurred at ~5723 eV was interpreted as arising from a combination of crystal-field splitting and excitation of different amounts of a Ce^{III} contaminant present in all the samples. For instance, the characteristic white line of a typical Ce^{III} compound, e.g., $Ce(NO_3)_3 \cdot 6H_2O$, is observed at the same energy as peak C.[31]

A significant change in the height of the jump at the white line was observed in the samples under study; that change could be a result of variation in the particle size of the solid samples. Similarly, variation in the L_{III}-edge XANES white line intensity as a function of the particle size has likewise been reported for nanocrystalline CeO_2[36] and Pt nanoparticle spectra.[37] X-ray diffraction patterns of both hydrous CeO_2 and **I** revealed a fluorite structure with a particle diameter of ~6 nm derived from the line broadening.[35] The particle diameter of anhydrous CeO_2 was larger than that of hydrous CeO_2 and **I**, whereas **II** was amorphous.[35] A cerium oxide precipitate prepared in a similar manner was found to be amorphous to X-rays but apparently comprised of nanocrystallites, <2 nm, as shown by transmission electron microscopy selected area electron diffraction.[38] The variation in particle size implied an altered particle nucleation in the presence of peroxide, perhaps related to induced site dislocations[39] as supported by EXAFS results below.

The cerium spectroscopic valence, νs, is defined as $\nu s = 3 + [I_A/(I_A + I_B)]$,[34] where I_A and I_B are the integrated areas under peaks A and B, respectively. The degree of 4f state occupation is then $nf = (4 - \nu s)$. Table 3 shows calculated values of both the f-electron count and the spectroscopic mixed valence of cerium in the samples under study. Similar results for anhydrous CeO_2 can also be found in previous reports.[21,23]

No significant change in the white line areas, as determined from the many-body configuration theory for a core transition to localized electronic states, was observed of the samples under study. Furthermore, changing the hydrogen peroxide concentration during the precipitation of cerium oxide did not result in a significant change in the electronic cerium mixed-valence state. These results are in agreement with X-ray photoelectron spectroscopy results[35] that showed different trivalent cerium contents but demonstrated differences in the initial and final electronic states of the complementary X-ray absorption techniques.

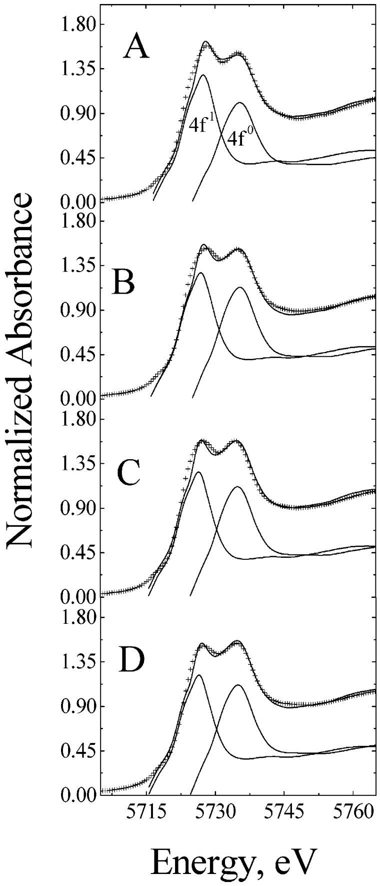

Figure 2. Ce L_{III}-edge XANES spectra with the calculated XANES spectra of (A) anhydrous CeO_2, (B) hydrous CeO_2, (C) sample **I**, and (D) sample **II**. Experimental data points are represented by (+), fitting model points by smooth curves.

Modeling of the XANES spectra, in terms of the one-electron band structure of the crystal for a core transition to delocalized electronic states, is a useful approach to determine the cerium valence state and support the results obtained from the many-body configuration theory for a core transition to localized electronic states. The full multiple scattering calculations of XANES features have been made using FEFF 8.20 code, Figure 2.[30] Though Tsvyashchenko et al.[40] concluded that the FEFF 8.1 code was unable to calculate XANES for cerium correctly, a modification was made in

---

(35) Schuman, T. Cerium oxide pigments for anti-corrosion primer coatings. Submitted for publication.

(36) Nachimuthu, P.; Shih, W.; Liu, R.; Jang, L.; Chen, J. *J. Solid State Chem.* **2000**, *149*, 408−413.

(37) Bazin, D.; Sayers, D.; Rehr, J. J.; Mottet, C. *J. Phys. Chem. B* **1997**, *101*, 5332−5336.

(38) Johnson, B. Y.; Edington, J.; O'Keefe, M. J. *Mater. Sci. Eng. A* **2003**, *361*, 225.

(39) Frank, F. C. *Discuss. Faraday Soc.* **1949**, *5*, 48.

(40) Tsvyashchenko, A. V.; Formicheva, L. N.; Sorokin, A. A.; Ryasny, G. K.; Komissarova, B. A.; Shpinkova, L. G.; Klementiev, K. V.; Kuznetsov, A. V.; Menushenkov, L. G.; Trofimov, V. N.; Primenko, A. E.; Cortes, R. *Phys. Rev. B* **2002**, *65*, 174513.

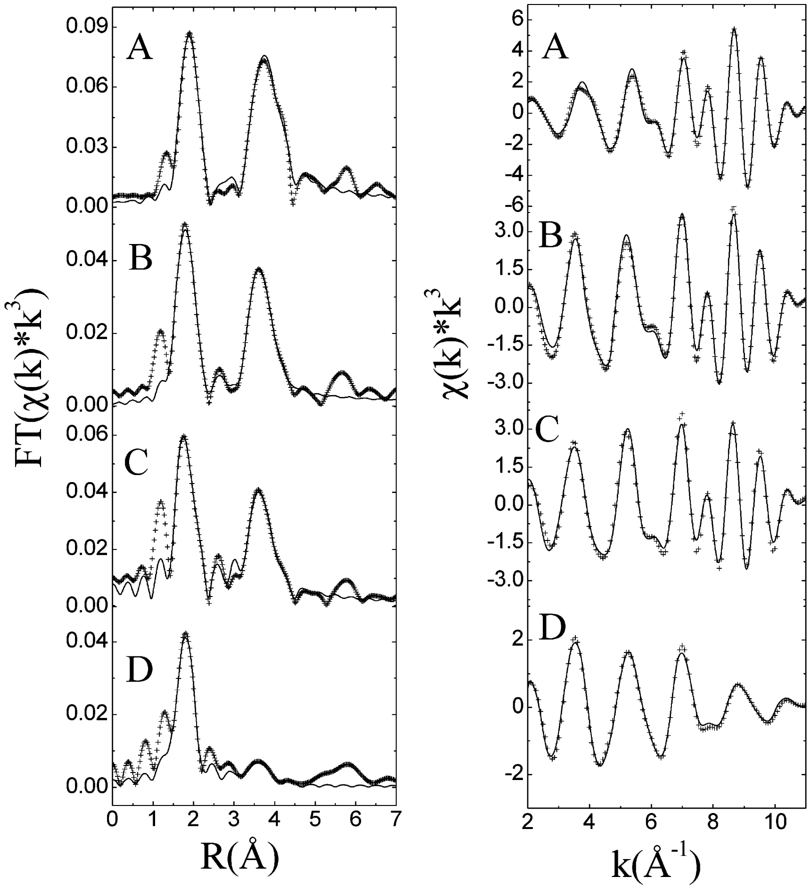

Figure 3. *R*-space fitting results for (A) anhydrous CeO_2, (B) hydrous CeO_2, (C) sample **I**, and (D) sample **II** EXAFS spectra. (Right) Corresponding Fourier-filtered data with back-transformed fitting function. Experimental data points are represented by (+), fitting model points by smooth curves.

the FEFF 8.20 code that permits a correctly calculated XANES for cerium. In the FEFF 8.20 code the default cerium ground and excited electronic states configurations are $4f^15d^0$ and L_{III} hole-$4f^25d^0$, respectively. Accordingly, the subroutine getorb in FEFF 8.20 code was modified in order to place the core−hole potential screening electron in the 5d orbital rather than the 4f orbital for the $4f^15d^0$ to L_{III} hole-$4f^15d^1$ transition and for the $4f^05d^0$ to L_{III} hole-$4f^05d^1$ transition.

The self-consistent potential calculations were carried out for a 7 Å cluster of cerium oxide and two different channels in order to account for the two ground-state electronic configurations. The first channel was due to the $2p_{3/2}4f^15d^0 \rightarrow L_{III}$ hole-$4f^15d^1$ transition, whereas the second was due to a $2p_{3/2}4f^05d^0 \rightarrow L_{III}$ hole-$4f^05d^1$ transition. The energy separation between the two channels was found to be of the order of ~8 eV, which is in agreement with the experimental values.

The broadening due to the experimental resolution was taken into account, and the weighting coefficients of the two channels were varied in order to obtain the best fit to the experimental data. Figure 2 shows the linear combinations of the two weighted XANES features with the experimental spectra. The calculated valences obtained from the XANES spectra simulation using FEFF 8.20 are in agreement with those obtained from the many-body configuration theory, Table 3.

EXAFS Spectral Results. Results of the fitting of the EXAFS spectra obtained from the two fitting models are summarized in Tables 1 and 2. Clearly, the fitting parameters obtained from the two fitting models were in good agreement regardless of which model was chosen. The extracted k^3-weighted EXAFS oscillations, the corresponding Fourier filtered data, and modeled EXAFS results for anhydrous CeO_2, hydrous CeO_2, **I**, and **II** are shown in Figure 3. For these samples, the extracted k^3-weighted EXAFS oscillations, Fourier filtered data, and modeled EXAFS results generated by the different fitting methods were practically indistinguishable, as evidenced by either the fitting parameters or the modeled spectral features within the error of the method. A pronounced component between 1 and 1.5 Å, representing a low-frequency contribution to the EXAFS, was likewise present in all spectra. The 1−1.5 Å component was not an artifact of the μ_0 spline function subtraction because it was persistent in the Fourier transform. Extreme μ_0 subtraction intolerably reduced the intensity of the Ce−O peak at $R - \Delta = 1.9$ Å. A Ce−O distance of less than 2 Å made no physical sense as the expected ionic radii is 2.34 Å for 6-fold coordination.[41] Furthermore, other Ce K-edge EXAFS found in the literature also demonstrate a low-*R* feature in the Fourier transform.[42,43]

---

(41) Greenwood, N. N.; Earnshaw, A. *Chemistry of the Elements*; VCH Verlagsgesellschaft: Weinheim, Germany, 1988.

(42) Lee, J.-F.; Tang, M.-T.; Shih, W. C.; Liu, R. S. *Mater. Res. Bull.* **2002**, *37*, 555−562.

(43) Nagai, Y.; Yamamoto, T.; Tanaka, T.; Yoshida, S.; Nonaka, T.; Okamoto, R.; Suda, A.; Sugiura, M. *Catal. Today* **2002**, *74*, 225−234.

Spectra of all the samples under study revealed an intense Fourier-transformed peak at 1.9 Å, corresponding to a phase-corrected R_{Ce}−O distance of about 2.3−2.5 Å. This feature represents oxygen that comprises the first coordination shell about a central absorbing cerium in each sample. The spectrum of crystalline anhydrous CeO_2 was modeled using single-scattering paths of the first three shells of cerium neighbors, i.e., the oxygen shell at 2.343 Å, the cerium shell at 3.826 Å, and a second oxygen shell at 4.486 Å. Crystallographic values for the fluorite structure of crystalline CeO_2 were reproduced within the typical range of EXAFS uncertainties.

The EXAFS spectrum of the amorphous precipitate (sample **II**) exhibited a different structure than that of either anhydrous CeO_2, hydrous CeO_2, or **I**. Above the spurious low-*R* feature, the major oxygen Fourier-transformed peak appeared dampened and had practically nonexistent outer-shell, Ce−Ce or Ce−O2, features. Addition of a second oxygen scattering path (O2) led to fitting **II** with 11.5 oxygen atoms at 2.401 Å and 2.5 further distant oxygen atoms at 3.331 Å. The number of oxygen atoms as second backscatterers was very small and associated with a large discrepancy in the Ce−O2 distance compared to anhydrous CeO_2.

Thus, modeling the Fourier transform using only a single shell of oxygen backscatterers, without including a second oxygen shell, resulted in the best qualitative fit. Using a single shell of oxygen backscatterers in modeling the Fourier transform from 1.5 to 2.9 Å did result in a necessary additional asymmetry term (third cumulant) for either fitting method. Models of **II** with a single oxygen-containing shell revealed that the oxygen atoms were located at a distance of 2.42 Å, which was significantly larger than that observed for anhydrous CeO_2. The increase of the Ce−O1 distance in **II** reflects a high σ^2 value and the necessity of allowing an additional anharmonic correction term for the O1 path. The additional anharmonic correction observation can reflect the presence of Ce−O bond lengths from different coordination oxygen atoms (−O−, OH_2).

Visual inspection of the hydrous CeO_2 and **I** spectra showed that the samples' near-neighbor structure deviated significantly from either anhydrous CeO_2 or **II**. The Ce−O1, Ce−Ce, and Ce−O2 neighbor coordinations in hydrous CeO_2 appeared more ordered with smaller σ^2 as compared with **I** or **II** but less ordered than the crystalline anhydrous CeO_2.

Precipitation of cerium oxide at the reduced H_2O_2 concentration resulted in precipitation of **I**. Analysis of the EXAFS spectrum of **I** indicated comparable oscillation amplitudes to those of hydrous CeO_2. The distance between cerium centers and oxygen neighbors in the first coordination shell are of similar magnitude, 2.360 and ∼2.364 Å for hydrous CeO_2 and **I**, respectively. However, larger deviations were observed in Ce−Ce and Ce−O2 distances between hydrous CeO_2 and **I**. Hydrogen peroxide thus induced changes in the coordination spheres around cerium, longer bond distances and fewer coordinated atoms.

Visual inspection of EXAFS spectra of both hydrous CeO_2 and **I** indicated that the first oxygen next-neighbor coordination shell in these two samples was most similar, but not identical, to anhydrous CeO_2. The parameters in the EXAFS analysis yielded higher *N*1 values, higher σ^2, and longer Ce−O bond distances for hydrous CeO_2, **I**, and, especially, **II** compared to anhydrous CeO_2. Increasing the coordination number, *N*1, was attributed to incorporation of H_2O molecules that resulted in a reduced crystalline order. Evaluation of each parameter in going from anhydrous CeO_2 to **II** indicates a decrease in crystalline order. The Fourier-transformed peak representing the Ce−Ce interaction of hydrous CeO_2 and **I** was more pronounced than in amorphous **II** and less pronounced than in crystalline anhydrous CeO_2. The enhanced Ce−Ce distance and the decreased coordination number, *N*2, in both hydrous CeO_2 and **I** compared with anhydrous CeO_2 were attributed to a higher degree of defect sites in these nanocrystalline materials.

In practice, enhanced corrosion protection of 7075 or 2024 aluminum alloy is observed for films synthesized in the presence of peroxide compared with a simple galvanic deposition. Rare earth coatings are primarily inhibitive of the oxygen reducing cathodic reaction and thus significantly retard the surface corrosion of aluminum.[9,10,12−15] This work suggested an altered film structure, composition, and particle size, which are associated with further retardation of oxygen permeation and consistent with an improved oxygen barrier, or trapping, film.[7,8,35,44]

Conclusions

The present study described the investigation of precipitated cerium oxide structures using conditions similar to those used in forming corrosion-preventive, cerium oxide films on aluminum alloys. Different hydrogen peroxide concentrations were employed during the precipitations of cerium oxide. We performed Ce L_{III}-edge XANES analyses in order to study the electronic configuration of cerium centers in the precipitated cerium oxide. Furthermore, the local atomic structure around cerium in the precipitated cerium oxides has been investigated using EXAFS and compared with two different standards, e.g., anhydrous CeO_2 and hydrous CeO_2.

XANES analysis clearly showed a significant change in the intensity of the white line peaks of precipitated cerium oxide, revealing a smaller particle size as compared to anhydrous CeO_2. However, no significant change in cerium spectroscopic valence for precipitated cerium oxides was observed, regardless of peroxide concentration, in comparison to the anhydrous CeO_2.

Precipitation of cerium oxide utilizing H_2O_2 resulted in an increased bond distance, R_{Ce-O}, as well as coordination number of the first coordination shell Ce−O. A decrease in the coordination numbers of the second shell, Ce−Ce, and third shell, Ce−O, were observed of the radial distribution functions. Furthermore, the Debye−Waller factors for the three shells exhibited a consistent trend as the values for the three coordination shells increased going from anhydrous CeO_2, hydrous CeO_2, sample **I,** to sample **II**. On the basis of these observations, the degree of disorder increased with increasing H_2O_2 concentration during precipitation of cerium oxide, consequently increasing the potential for cerium oxide

---

(44) Sangaj, N. S.; Malshe, V. C. *Prog. Org. Coatings* **2004**, *50*, 28.

precipitates to function as oxygen traps. Decreasing the particle size of cerium oxide precipitates, with a probable increase in oxygen trapping capability, offers additional insight into the enhancement of the corrosion protection of aluminum substrates by cerium oxide films.

Acknowledgment. This project was in collaboration with the cerium project group at the Materials Research Center of the University of Missouri—Rolla, with Drs. James Stoffer, Thomas O'Keefe, Matthew O'Keefe, William Fahrenholtz, and Paul Yu, and Mr. Scott Hayes. Raphaël P. Hermann provided helpful suggestions on modification of the FEFF 8.20 code. Support for the project was provided through the Air Force Research Laboratory Materials and Manufacturing Directorate, project manager Steve Szaruga. Portions of this research were carried out at the Stanford Synchrotron Radiation Laboratory (SSRL), a national user facility operated by Stanford University on behalf of the U.S. Department of Energy, Office of Basic Energy Sciences. The SSRL Structural Molecular Biology Program is supported by the Department of Energy, Office of Biological and Environmental Research, and by the National Institutes of Health, National Center for Research Resources, Biomedical Technology Program.

CM0492437